

## Nonlinear saturated states of the magnetic-curvature-driven Rayleigh–Taylor instability in three dimensions

Amita Das, Abhijit Sen, Predhiman Kaw, S. Benkadda, and Peter Beyer

Citation: *Physics of Plasmas* **12**, 032302 (2005); doi: 10.1063/1.1850476

View online: <http://dx.doi.org/10.1063/1.1850476>

View Table of Contents: <http://scitation.aip.org/content/aip/journal/pop/12/3?ver=pdfcov>

Published by the *AIP Publishing*

---

### Articles you may be interested in

[Electromagnetic fluid drift turbulence in static ergodic magnetic fields](#)

*Phys. Plasmas* **12**, 122308 (2005); 10.1063/1.2141928

[On the transition to drift turbulence in a magnetized plasma column](#)

*Phys. Plasmas* **12**, 052320 (2005); 10.1063/1.1889443

[Erratum: Nonlinear saturated states of the magnetic-curvature-driven Rayleigh–Taylor instability in three dimensions \[\*Phys. Plasmas\* \*\*12\*\*, 032302 \(2005\)\]](#)

*Phys. Plasmas* **12**, 059901 (2005); 10.1063/1.1887685

[Rayleigh–Taylor instability driven nonlinear vortices in dusty plasmas](#)

*Phys. Plasmas* **12**, 044506 (2005); 10.1063/1.1881452

[Zonal and streamer structures in magnetic-curvature-driven Rayleigh–Taylor instability](#)

*Phys. Plasmas* **8**, 5104 (2001); 10.1063/1.1416483

---



## VACUUM SOLUTIONS FROM A SINGLE SOURCE

Pfeiffer Vacuum stands for innovative and custom vacuum solutions worldwide, technological perfection, competent advice and reliable service.

# Nonlinear saturated states of the magnetic-curvature-driven Rayleigh–Taylor instability in three dimensions

Amita Das, Abhijit Sen, and Predhiman Kaw  
*Institute For Plasma Research, Bhat, Gandhinagar 382428, India*

S. Benkadda and Peter Beyer  
*Equipe Dynamique des Systemes Complexes, 13397 Marseille, France*

(Received 29 June 2004; accepted 19 November 2004; published online 3 February 2005)

Three-dimensional electromagnetic fluid simulations of the magnetic-curvature-driven Rayleigh–Taylor instability are presented. Issues related to the existence of nonlinear saturated states and the nature of the temporal evolution to such states from random initial conditions are addressed. It is found that nonlinear saturated states arising from generation of zonal shear flows continue to exist in certain parametric domains but their spectrum and spatial characteristics have important differences from earlier two-dimensional results reported in *Phys. Plasmas* **4**, 1018 (1997) and *Phys. Plasmas* **8**, 5104 (2001). In particular, the three-dimensional nonlinear states possess a significant power level in short scales and the spatial structures of the potential and density fluctuations appear not to develop any functional correlations. Electromagnetic effects are found to inhibit the formation of zonal flows and thereby to considerably restrict the parametric domain of nonlinear stabilization. The role of finite  $k_{\parallel}$  and the contribution of the unstable drift wave branch are also discussed and delineated through a number of simulation studies carried out in special simplified limits. © 2005 American Institute of Physics. [DOI: 10.1063/1.1850476]

## I. INTRODUCTION

The magnetic-curvature-driven Rayleigh–Taylor (MCD-RT) model is a useful paradigm for the study of long wavelength nonlinear shear flow patterns such as zonal flows and streamer structures.<sup>1,2</sup> These coherent potential patterns are believed to play an important role in determining the turbulent transport of matter and heat across field lines in magnetically confined plasma devices such as tokamaks, stellarators, etc.<sup>3–12</sup> In the past few years a large number of investigations have been devoted to the elucidation of their characteristics and in understanding their contributions towards transport processes.<sup>3–12</sup> In the tokamak context, theoretical studies have mainly centered around the drift-wave model or its several variants such as the ion temperature gradient mode, the electron temperature gradient mode,<sup>13–15</sup> etc. The basic physics underlying the formation of these nonlinear structures is the onset of a long scale modulational instability arising from the nonlinear parametric interaction of a large number of short scale fluctuations; this mechanism is in essence common to a number of earlier model calculations of strong plasma turbulence including that of the coupled interaction of Langmuir waves and ion-acoustic excitations.<sup>16</sup> In a recent work<sup>1</sup> the MCD-RT model was used to explore a very fundamental question pertaining to the formation of these nonlinear patterns, namely, what determines the symmetry of the final state—whether one gets zonal flows or streamer formations.<sup>1</sup> The study highlighted the role of dissipative processes (namely, the strength of the dissipation parameters—the flow viscosity  $\mu$  and the diffusion coefficient  $D$ ) in influencing the evolutionary path of the system towards a particular final symmetry state. Using extensive numerical simulation data it was possible to con-

struct a consolidated “phase diagram” in  $D$ - $\mu$  space which showed that low dissipation favored the formation of zonal flows leading to saturated stationary states whereas high dissipation led to formation of radially elongated streamer flow patterns. The primary impact of the dissipation was on the initial evolution of the short scale fluctuations and the consequent distribution of their spectral power. High power in the short scales (due to weak dissipation) at the initial stages led to stronger nonlinear generation of zonal flows whereas for high dissipation the streamers gained an upper hand and zonal flows were subdominant. We believe that such a unified and consolidated approach could be useful in gaining understanding of the evolution of similar nonlinear structures in tokamak transport models as well. Motivated by such considerations and also keeping in mind the fact that the RT model in a generic sense can provide valuable insights in a number of other experimental scenarios (e.g., currentless toroidal devices, ionospheric spread  $F$  irregularities, etc.) we extend and further develop explorations on the nonlinear dynamics of this model. The earlier results reported in Refs. 1 and 2, were based on two-dimensional simulations. In this paper we report a major extension of this model by making it fully three dimensional and also by including electromagnetic effects through the contributions of magnetic fluctuations. In terms of basic physics the extended model now introduces linear and nonlinear coupling to shear Alfvén modes through finite  $k_{\parallel}$  effects so that we now have a set of three coupled nonlinear equations that evolve the scalar electric field potential  $\phi$ , the plasma density  $n$ , and the parallel component of the magnetic vector potential  $\psi$ . We also have an additional dissipation parameter in the form of the resistivity coefficient  $\eta_s$  which makes the drift-wave branch linearly unstable in certain parameter ranges. We continue to

explore the same fundamental issues in this generalized model, namely, the existence of saturated nonlinear states, their characteristics, and the factors that influence their formation. Our approach is primarily numerical and we present extensive simulation results from our model equations to provide answers to the above issues. On the question of the existence of saturated states, past results from numerical explorations of the drift wave and allied models have been somewhat equivocal and have indicated that electromagnetic effects tend to inhibit zonal flow development. In our numerical simulations of the fully electromagnetic RT model we find that saturated states still continue to, exist although in a restricted parameter domain. Comparison with the earlier two-dimensional results show a similarity in the saturation mechanism, namely, through the excitation of zonal flows. However, there are significant differences in some of the characteristics of the saturated states. Thus the three-dimensional nonlinear states are found to possess a significantly higher power level in short scales as compared to their two-dimensional (2D) counterparts. Another significant difference is that the spatial structures of the potential and density fluctuations do not develop any functional correlations. In other words, unlike in the 2D case, the density evolution does not slave itself to the potential evolution. Our findings on the effect of electromagnetic fluctuations on RT turbulence are similar to those of drift-wave models, namely, that they tend to inhibit the formation of zonal flows and thereby to considerably restrict the parametric domain of nonlinear stabilization. To highlight the role of the third dimension we have also explored a simplified limit of our model that can be termed as a three-dimensional electrostatic model. In this simplified model the role of  $k_{\parallel}$  and the resistivity factor  $\eta_s$  are more transparent and we discuss their influence in the formation dynamics of the saturated states. In this limit we also demonstrate the stabilizing influence of the secondary Kelvin–Helmholtz instability<sup>17</sup> in controlling the unlimited growth of streamers.

The paper is organized as follows. In the following section we present our generalized model equations and discuss its characteristics including its relation to the previous 2D model equations. We also derive a simplified limit of two coupled equations representing the three-dimensional electrostatic model. Section III is devoted to delineating the properties of the linear modes of the model. This is done through numerical and approximate analytic solutions of the appropriate dispersion relations in various limits. This analysis also highlights the role of the various dissipation parameters and the parallel wavelength in the linear evolution stage of the system. We next present our nonlinear simulation results on the 3D electrostatic model in Sec. IV and compare and contrast them with past 2D electrostatic results. The full electromagnetic simulation results of the generalized model are presented and discussed in Sec. V. The paper ends with a summary of our main results and some concluding remarks in Sec. VI.

## II. MODEL EQUATIONS

The governing equations for the generalized model of the magnetic-curvature-driven Rayleigh–Taylor instability are similar to those investigated earlier by Kaw [see Ref. 18] and can be derived along similar lines to that adopted for the previously investigated two-dimensional set of equations (1) and (2). We sketch here the main steps of the derivation with the details being given in the Appendix. We use the fluid equations of continuity and momentum for the electrons and ions along with the quasineutrality condition, viz.,  $\nabla_{\perp} \cdot \vec{J}_{\perp} = -\nabla_{\parallel} J_{\parallel}$ . In addition we close the set by the Ohm's law which is the parallel component of the electron momentum equation without the electron inertia term. We use a slab representation (its validity has been discussed in detail in the Appendix) in which the radial coordinate is represented by  $x$ , the poloidal by  $y$ , and the toroidal by  $z$ . We choose the equilibrium  $x$  dependent toroidal magnetic field as  $\vec{B}_{eq} = B_0(1 - x/R)\hat{z}$ . The radial gradient of the equilibrium plasma density is represented by  $n_0(x) = n_{00}\exp(-x/L_n)$ . We take the ions to be cold ( $T_i = 0$ ) but retain a finite electron temperature  $T_e$ . As a result of this the ion drift (flow) in equilibrium is zero but there is an equilibrium electron diamagnetic drift in the direction perpendicular to the magnetic field. This electron diamagnetic drift leads to a current  $\vec{J} = -\nabla p_{e0} \times \vec{B}/B^2$  in  $y$  (poloidal) direction in equilibrium. For an infinite periodic slab system considered here the condition for equilibrium is identically satisfied as  $\vec{J} \times \vec{B} = \nabla p_{e0}$ . In a finite toroidal system the divergence of diamagnetic drift leads to a charge separation. The consequent  $\vec{E} \times \vec{B}$  drift can then throw the plasma out. For finite system the equilibrium is thus system specific and is achieved by a variety of means, e.g., insertion of a conducting aperture and/or a poloidal field lines (as in tokamaks) to short out the charge separation.

Unlike the 2D model, in the three-dimensional case here, we retain electromagnetic perturbations ( $\vec{B} = \vec{B}_{eq} + \hat{z} \times \nabla \psi$ ), where the perturbed magnetic field fluctuations are assumed to arise only from magnetic field line bending perturbations. Thus the vector potential has only a  $\hat{z}$  component, i.e.,  $\vec{A} = -\psi\hat{z}$ . The electric field is given by  $\vec{E} = -\nabla\phi + (1/c)\partial\psi/\partial t\hat{z}$ . The scalar and vector potentials are finite only for the perturbations. The total density is  $N = n_0 + n_1$ , thus  $\ln N = -x/L_n + \ln(1 + n_1/n_0) = -x/L_n + n$ . The unit vector parallel to the magnetic field is given by  $e_{\parallel} = \vec{B}/|B_0| = \hat{z} + (\hat{z} \times \nabla\psi)/B_0$ . From standard perturbative expansions, the perpendicular component of the electron momentum equation yields the usual transverse flow velocities, namely, the  $\vec{E} \times \vec{B}$  drift and the diamagnetic drift. The ion equation similarly leads to a  $\vec{E} \times \vec{B}$  drift term as well as a polarization drift contribution in the perpendicular direction. These are substituted in the subsequent order equations to obtain the nonlinear evolution equations. We express the equations in a dimensionless form by normalizing the various physical quantities as follows. The density is normalized by  $n_{00}$ , the electrostatic potential  $\phi$  by  $T_e/e$ , time by  $\Omega_i$ , and length by  $\rho_s = c_s/\Omega_i$ . The vector potential  $\psi$  is normalized by  $B_0\rho_s$ . Our generalized set of model equations then consist of the fol-

lowing three coupled equations for the plasma density  $n$ , scalar electrostatic potential  $\phi$ , and the parallel (to the equilibrium magnetic field  $\vec{B}_{eq}$ ) component of the vector potential  $\psi$ ,

$$\frac{\partial n}{\partial t} + V_g \frac{\partial n}{\partial y} + (V_n - V_g) \frac{\partial \phi}{\partial y} + \hat{z} \times \vec{\nabla} \phi \cdot \vec{\nabla} n - V_A^2 \times \left\{ \frac{\partial}{\partial z} \nabla_{\perp}^2 \psi + \hat{z} \times \vec{\nabla} \psi \cdot \vec{\nabla} \nabla_{\perp}^2 \psi \right\} = D \nabla^2 n, \quad (1)$$

$$\frac{\partial}{\partial t} \nabla^2 \phi + V_g \frac{\partial n}{\partial y} + \hat{z} \times \vec{\nabla} \phi \cdot \vec{\nabla} \nabla^2 \phi - V_A^2 \times \left\{ \frac{\partial}{\partial z} \nabla_{\perp}^2 \psi + \hat{z} \times \vec{\nabla} \psi \cdot \vec{\nabla} \nabla_{\perp}^2 \psi \right\} = \mu \nabla^4 \phi, \quad (2)$$

$$\frac{\partial \psi}{\partial t} + \frac{\partial}{\partial z} (n - \phi) + V_n \frac{\partial \psi}{\partial y} - \hat{z} \times \vec{\nabla} \psi \cdot \vec{\nabla} (\phi - n) = \eta_s V_A^2 \nabla_{\perp}^2 \psi. \quad (3)$$

Here  $V_g = c_s / (R \Omega_i)$  is the gravitational drift arising through the magnetic curvature terms,  $V_n = c_s / (L_n \Omega_i)$  is the diamagnetic drift speed,  $c_s$  is the ion acoustic speed,  $R$  is the major radius of curvature,  $\Omega_i$  is the ion cyclotron frequency,  $L_n$  is the equilibrium density scale length, and  $\mu$  and  $D$  are the dynamical viscosity and the diffusion coefficient, respectively. Here  $V_A$  is the Alfvén velocity normalized to the sound velocity ( $V_A^2 = v_a^2 / c_s^2$ ). Thus the plasma  $\beta$  can be expressed as  $\beta = 1 / V_A^2$ . The coefficient of resistivity defined as  $\eta_s = \nu (c^2 / \omega_p^2) (\omega_{ci} / v_a^2) = (\nu / \omega_p) (\omega_{ci} / \omega_p) (c^2 / v_a^2) = \nu / \omega_{ce}$  is a dimensionless parameter. Thus,  $\eta_s = 1.6 \times 10^{-13} n \ln(\Lambda) / B T_e^{3/2}$ , here  $n$  is the plasma density,  $B$  is the magnetic field in cgs system of units,  $T_e$  is the electron temperature in eV, and  $\ln(\Lambda)$  is the Coulomb logarithm. In the present work we discuss in detail the linear and nonlinear features exhibited by these set of equations.

Comparing Eqs. (1) and (2) to our earlier 2D model equations, we see that the extended model has additional linear and nonlinear coupling to the magnetic perturbation. The coupling coefficient is proportional to  $V_A^2$  (i.e., inversely proportional to  $\beta$ ) as well as to the spatial variation in the parallel direction (i.e., to  $k_{\parallel}$ ). Equation (3) describes the time evolution of the magnetic fluctuation and is coupled both to the density and potential fluctuations. In terms of basic physics the generalized model has an additional collective degree of freedom, namely, the shear Alfvén modes and finite  $k_{\parallel}$  effects bring about a linear and nonlinear coupling between them and the RT and drift modes. We also have an additional dissipation parameter in the system, namely, the resistivity coefficient  $\eta_s$  appearing in the Ohm's law. We will discuss the linear properties of the model in greater detail in the following section.

Note that the two-dimensional limit can be obtained by putting  $\partial / \partial z \rightarrow 0$  for which Eqs. (1) and (2) are not influenced in any way by the electromagnetic perturbations. Although the evolution of  $\psi$  through Eq. (3) is driven by  $n$  and  $\phi$ , but  $\psi$  is unable to react back on  $n$  and  $\phi$  fields. Also in this limit, it is easy to show from Eq. (3) that the mean

square vector potential ( $\sim \int |\psi|^2 d^3 r$ ) simply decays away at a rate proportional to  $\eta_s V_A^2$ . So in the two-dimensional limit the electromagnetic perturbations have no role to play in the evolution of  $n$  and  $\phi$ . Even when 3D effects are important the electromagnetic effects can be negligible. This will happen when the evolution of  $\psi$  becomes unimportant but the parallel current continues to remain finite and provides coupling to finite  $k_z$  modes in the evolution equations for density and potential. Such a limit is possible when  $\eta_s V_A^2 \nabla^2 \psi \gg \partial \psi / \partial t$  (or  $\eta_s V_A^2 k_{\perp}^2 \gg \gamma$ , the growth rate). The requisite limiting procedure thus consists of letting  $\psi \rightarrow 0$  but letting the parallel current contribution (proportional to  $\nabla_{\perp}^2 \psi$ ) on the right-hand side of Eq. (3) remain finite. Thus from Eq. (3) we have,

$$\nabla_{\perp}^2 \psi = \frac{1}{\eta_s V_A^2} \frac{\partial}{\partial z} (n - \phi). \quad (4)$$

Substituting for  $\nabla_{\perp}^2 \psi$  in Eqs. (1) and (2) we obtain,

$$\frac{\partial n}{\partial t} + V_g \frac{\partial n}{\partial y} + (V_n - V_g) \frac{\partial \phi}{\partial y} + \hat{z} \times \vec{\nabla} \phi \cdot \vec{\nabla} n - \frac{1}{\eta_s} \times \left\{ \frac{\partial^2}{\partial z^2} (n - \phi) \right\} = D \nabla^2 n, \quad (5)$$

$$\frac{\partial}{\partial t} \nabla^2 \phi + V_g \frac{\partial n}{\partial y} + \hat{z} \times \vec{\nabla} \phi \cdot \vec{\nabla} \nabla^2 \phi - \frac{1}{\eta_s} \left\{ \frac{\partial^2}{\partial z^2} (n - \phi) \right\} = \mu \nabla^4 \phi. \quad (6)$$

We will refer to the above two coupled set of evolution equations [Eqs. (5) and (6)] as the 3D electrostatic model. The set of Eqs. (5) and (6) are considerably simplified in comparison with Eqs. (1)–(3). They describe the coupling between only two variables, viz., density and the scalar potential with no electromagnetic effects. However, the influence of the third dimension is still present through  $\partial / \partial z$  for finite values of the parallel component of the wave vector  $k_{\parallel}$ . Physically, this simplified limit can be understood as follows. The perpendicular variation of the Rayleigh–Taylor mode produces the charging of magnetic field lines via the polarization drift effect. Finite spatial variation in the parallel direction implies that the magnetic field line is charged differently at different points thereby promoting the flow of a parallel current. The magnetic field associated with this current is responsible for the electromagnetic perturbations. However, if the resistivity of the plasma is high ( $\eta_s V_A^2 k_{\perp}^2 \gg \gamma$  the linear growth rate), such a parallel current gets heavily damped, consequently the magnetic field as well as the creation of the rotational electric field  $\partial \psi / \partial t$  is negligible (and hence the limit  $\psi \rightarrow 0$ ). The perturbations are therefore essentially electrostatic in nature in this limit and hence can be considered as an appropriate three-dimensional extension of the earlier 2D electrostatic model. It provides a simple means of carrying out a direct comparison with the 2D results in the presence of finite  $k_{\parallel}$  and finite resistivity effects.

In the absence of  $V_g$ , the gravitational drift, the 3D electrostatic model equations (5) and (6) reduces to the well-known Hasegawa–Wakatani model,<sup>19</sup> studied in great detail for the understanding of electrostatic low frequency plasma



turbulence phenomena in three dimensions. Its 2D variants, obtained by replacing  $z$  derivative by a single scalar number has also attracted considerable attention.<sup>19</sup>

There is an interesting scaling property displayed by both 3D electrostatic as well as the generalized 3D electromagnetic equations which we now wish to highlight. The equations remain invariant under the following scaling transformations:

$$z \rightarrow \bar{z}/a; \quad \eta_s = a^2 \bar{\eta}_s; \quad \psi = a \bar{\psi}; \quad V_A^2 = \bar{V}_A^2/a^2. \quad (7)$$

Here  $a$  is a scalar scaling factor. These scalings help in establishing equivalence amidst a wide class of phenomena for which the parameters  $\beta$ ,  $\eta_s$ , and the typical length scales along the equilibrium magnetic field direction are related according to the above mentioned scaling relations. Note that the transformation leaves  $k_z V_A$ ,  $\psi V_A$ , and  $\eta_s V_A^2$  invariant. It also leaves the total energy (as well as each of the individual components of energy, namely, pressure, kinetic energy, and the magnetic energy) as invariant. Although the field  $\psi$  gets scaled, yet the magnetic energy (normalized to plasma thermal energy, viz.,  $\bar{b}^2/8\pi nT$ ) which is  $\int (\nabla \psi)^2 d^3r / (2\beta \int d^3r) = V_A^2 \int (\nabla \psi)^2 d^3r / (2 \int d^3r)$  in our normalizations, remains invariant. The scaling relationship helps in carrying out simulation for a convenient choice of the set of parameters  $\beta$ ,  $\eta_s$ , and  $L_z$  (the box length along the  $\hat{z}$  direction which defines the typical size of the excitation scales along  $\hat{z}$ ), which can later be related to the realistic set of values using the scaling coefficient  $a$ .

We will explore the nonlinear states of the 3D electrostatic model set equations (5) and (6) as well as the full generalized electromagnetic set given by Eqs. (1)–(3) in Secs. IV and V after discussing their linear properties in the following section.

### III. LINEAR ANALYSIS

The coupled set of equations (1)–(3) can be linearized and fourier analyzed to obtain the following dispersion relation:

$$\begin{aligned} & -ik_{\perp}^2 \omega^3 + \{(D + \mu + \eta_s V_A^2)k_{\perp}^4 + ik_{\perp}^2 k_y (V_g + V_n)\} \omega^2 \\ & + \{i(D \eta_s V_A^2 + D\mu + \eta_s V_A^2 \mu)k_{\perp}^6 + ik_{\perp}^2 V_A^2 k_{\perp}^2 (1 + k_{\perp}^2)\} \omega \\ & + \{-k_{\perp}^4 k_y [(\eta_s V_A^2 + \mu)V_g + (D + \mu)V_n] + ik_{\perp}^2 (V_g^2 \\ & - V_g V_n - k_{\perp}^2 V_g V_n)\} \omega - D \eta_s V_A^2 \mu k_{\perp}^8 - (D \\ & + \mu k_{\perp}^2)k_{\perp}^2 V_A^2 k_{\perp}^4 - i\mu k_{\perp}^6 k_y (\eta_s V_A^2 V_g + DV_n) \\ & + ik_{\perp}^2 k_z^2 V_A^2 k_y (V_g - V_n) - \eta_s V_A^2 k_{\perp}^2 k_y^2 V_g (V_g - V_n) \\ & + \mu k_{\perp}^4 k_y^2 V_n V_g - ik_y^3 V_g^2 V_n + ik_y^3 V_g V_n^2 = 0. \end{aligned} \quad (8)$$

The above dispersion relation contains three basic modes, namely, the drift wave, the Rayleigh–Taylor mode, and the shear-Alfvén wave. This can be seen quite easily by setting all the dissipative coefficients to be zero (i.e.,  $D = \mu = \eta_s = 0$ ) and by rearranging Eq. (8) in the following form:

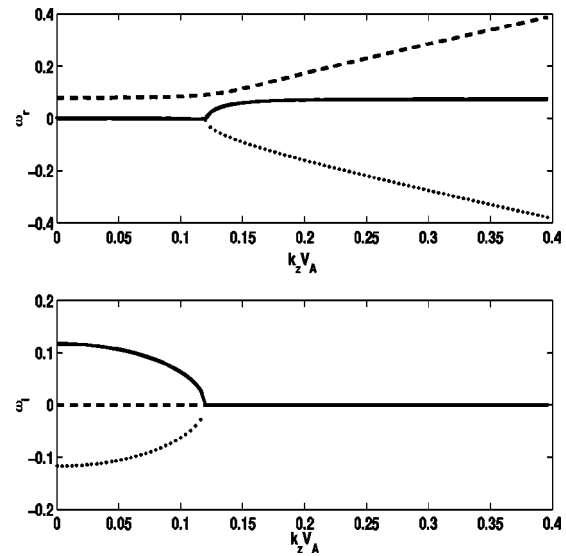


FIG. 1. Plot of the real frequency  $\omega_r$  and the growth rate  $\omega_i$  vs  $k_z V_A$  for the electromagnetic dispersion relation of Eq. (8) in the nondissipative limit, i.e., for  $D = \mu = \eta_s = 0$ . The other parameters are  $V_g = 0.036$  and  $V_n = 0.8$ . The perpendicular scales are  $k_x = k_y = 0.1$ .

$$\begin{aligned} & (\omega - k_y V_n) \left\{ \omega^2 - k_y V_g \omega + \frac{k_y^2}{k_{\perp}^2} V_g (V_n - V_g) \right\} \\ & = k_z^2 V_A^2 (1 + k_{\perp}^2) \left\{ \omega + \frac{k_y (V_g - V_n)}{(1 + k_{\perp}^2)} \right\}. \end{aligned} \quad (9)$$

For  $V_g = V_n = 0$  (i.e., in the absence of magnetic curvature and density gradients) Eq. (9) gives the kinetic Alfvén wave dispersion relation,

$$\omega^2 = k_z^2 V_A^2 (1 + k_{\perp}^2). \quad (10)$$

When  $V_n$  is finite,  $V_g = 0$  and  $V_A^2 \rightarrow \infty$  (a low  $\beta$  plasma) we have upon dividing Eq. (9) by  $V_A^2$ ,

$$\omega = \frac{k_y V_n}{(1 + k_{\perp}^2)}, \quad (11)$$

which is the drift-wave dispersion relation. For this case the electrons have a Boltzmann distribution, i.e., the wave time scales are in the regime of  $\omega/k_z v_{th,e} < 1$ . The two-dimensional electrostatic Rayleigh–Taylor growth rate can be recovered by putting  $k_z^2 V_A^2 \rightarrow 0$  in Eq. (9),

$$\left\{ \omega^2 - k_y V_g \omega + \frac{k_y^2}{k_{\perp}^2} V_g (V_n - V_g) \right\} = 0. \quad (12)$$

For this mode the electrons act like a two-dimensional fluid, under the condition of  $\omega/k_z v_{th,e} > 1$ . This is the only mode which is unstable (has a finite growth rate) in the nondissipative limit. At a finite value of  $k_z V_A$  this unstable mode gets coupled to the stable Alfvén branch. We show in Fig. 1 the variation of the real and imaginary parts of  $\omega$  as a function of  $k_z V_A$ . The value of  $k_x = k_y = 0.1$  has been chosen for the plot. The other parameters are  $V_g = 0.036$ ,  $V_n = 0.8$ ,  $D = \mu = \eta_s = 0$ . For small values of  $k_z V_A$  we observe that the three roots of the cubic equation are essentially obtained by putting the right-hand side of Eq. (9) to be zero. This gives rise to one

real root  $\omega = k_y V_n$  (arising due to the balance between the parallel electric field and the equilibrium pressure variation along the bent magnetic field lines), and two complex roots of the Rayleigh–Taylor mode. For the parameters  $k \ll 1$  (scale lengths longer than  $\rho_s$ ) we have ( $\omega = \omega_r + i\omega_i$ )

$$\omega_i = \pm \frac{1}{2} \left\{ 4 \frac{k_y^2}{k_\perp^2} V_g (V_n - V_g) - k_y^2 V_g^2 \right\}^{1/2}$$

$$\approx \pm \frac{k_y}{k_\perp} \sqrt{V_g (V_n - V_g)},$$

$$\omega_r = \frac{1}{2} k_y V_g.$$

Clearly, for a choice of  $V_g \ll V_n$  the real part of the frequency is much smaller than the growth rate, i.e.,  $\omega_r \ll \omega_i$  and is negligible as the plot of Fig. 1 in the regime of small  $k_z V_A$  shows. As  $k_z V_A$  increases the right-hand side of Eq. (9) cannot be ignored. Figure 1 shows that with increasing  $k_z V_A$ ,  $|\omega_i|$  decreases and goes to zero at  $k_z V_A = k_{zc} V_A$ . The point  $k_z = k_{zc}$  is in fact the point of exchange of instability, as  $\omega_r \approx 0$  remains close to zero up to this point for the Rayleigh–Taylor branch and becomes finite for values of  $k_z V_A > k_{zc} V_A$ . The expression for  $k_{zc}$  can thus be determined from Eq. (9) by substituting  $\omega = 0$ . This gives

$$k_{zc} = k_y \sqrt{V_n V_g / V_A} k_\perp. \quad (13)$$

The critical wave number  $k_{zc}$ , beyond which the growth rate vanishes, thus increases with increasing values of  $V_n$ ,  $V_g$ , and  $k_y$  but decreases with increasing values of  $V_A$  and  $k_\perp$ . For the values chosen for these parameters in Fig. 1 we have  $k_{zc} V_A = 0.12$ . The limit on  $k_z$  for instability is in fact identical to the threshold condition on plasma  $\beta$  encountered in the context of ideal magnetohydrodynamic ballooning modes in toroidal devices such as tokamaks. In the ballooning mode case, one generally seeks the critical value of of plasma beta ( $\beta = \beta_c$ ), beyond which the instability sets in for a fixed value of the parallel wave number. Here, on the other hand, we have fixed the value of  $\beta$  and are seeking the threshold condition on  $k_z$  the parallel wave number below which the instability exists. This has been done keeping in view the identification of the linearly unstable modes for the three-dimensional simulations, where a range of  $k_z$  are present and  $\beta = 1/V_A^2$  would be taken as a parameter. However, the expression for  $\beta_c$  encountered in the context of ballooning modes can be recovered from Eq. (13) by substituting  $k_{zc} = 1/qR$ ,  $k_y \sim k_\perp$ ,  $1/V_A^2 = \beta_c$ ,  $V_n V_g = 1/RL_n = 1/Ra$ , (as the density gradient scale length  $L_n$  can be taken typically to be of the order of minor radius  $a$ ). These substitutions in Eq. (13) then lead to the well-known expression for the critical value of plasma beta as  $\beta_c = a/q^2 R = \epsilon/q^2$ , where  $\epsilon$  is the aspect ratio.

In the region  $k_z < k_{zc}$  the curve  $\omega_i$  vs  $k_z$  in Fig. 1 typically seems to have an elliptical shape. This can be understood as follows, we know that in this region  $\omega_r \rightarrow 0$ , hence  $\omega^2 = -\omega_i^2$ . Considering the regions where  $\omega_i < k_y V_n$  and using  $V_g \ll V_n$  we write the dispersion relation as

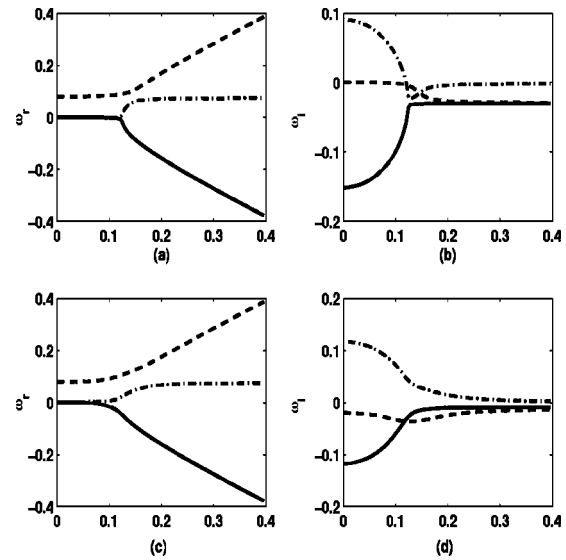


FIG. 2. Plot of real frequency and the growth rate from the dispersion relation of Eq. (8) as a function of  $k_z V_A$  when  $\mu = 3$  is finite [subplots (a) and (b)] and when  $\eta_s V_A^2 = 1.6$  is finite [subplots (c) and (d)]. The other parameters are same as that of Fig. 1.

$$\omega_i^2 + k_z^2 V_A^2 - \frac{k_y^2}{k_\perp^2} V_g V_n = 0 \quad (14)$$

i.e.,

$$\omega_i^2 + (k_z^2 - k_{zc}^2) V_A^2 = 0,$$

which is an equation of an ellipse. Interestingly, the dispersion relation simplifies to similar elliptic form as of Eq. (14) for  $\omega_i > k_y V_n$ , with the only modification that in this case the term  $k_z^2 V_A^2$  is multiplied by the factor of  $(1 + k_\perp^2)$ .

There are certain other features exhibited by the plot of Fig. 1. The only root which has the finite real part at  $k_z = 0$  is  $\omega_r = k_y V_n$ , and arises from the decoupled  $\psi$  equation in this limit; at higher  $k_z$  it approaches the stable shear-Alfvén branch with  $\omega_r = k_z V_A$ . This mode remains stable throughout, the imaginary part of this particular mode remains = 0 in the entire  $k_z$  domain. The real part of the both RT branches are zero for  $k_z < k_{zc}$ ; however, as  $k_z$  is increased beyond  $k_{zc}$ , one amongst them asymptotes towards the drift-wave dispersion relation  $\omega_r = k_y V_n / (1 + k_\perp^2)$  and the other approaches the complementary branch of the shear-Alfvén mode, i.e.,  $\omega = -k_z V_A$ .

We now investigate the effect of dissipation on the frequency as well as on the growth rate of the three modes. In Fig. 2 we have plotted the growth rate and the real frequency with  $k_z V_A$  when the dissipative coefficients  $\mu$  [subplots (a) and (b)] and  $\eta_s$  [subplots (c) and (d)] are separately taken to be finite. A comparison with the corresponding nondissipative case (all other parameters being identical) of Fig. 1, clearly shows that a finite value of  $\mu$  does not alter the real frequency and the threshold condition on  $k_z V_A$  significantly. It, however, causes an overall reduction in growth rate. An entirely different and interesting trend is observed with respect to the dissipative coefficient  $\eta_s$ . As the value of  $\eta_s$  is increased the real frequency instead of suddenly acquiring a finite value beyond  $k_z V_A = k_{zc} V_A$ , gradually starts deviating

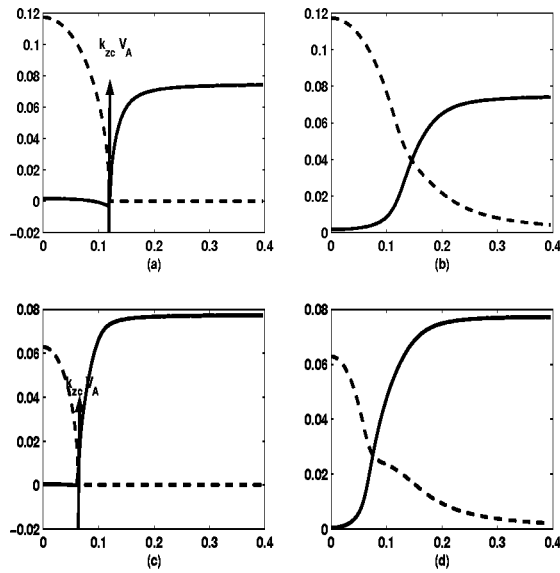


FIG. 3. The plot of real (solid lines) and imaginary (dashed lines) parts of the frequency for the resistivity driven branch. The ideal results for  $\eta_s=0$  are plotted in subplot (a) ( $V_g=0.0364$ ) and subplot (c) ( $V_g=0.01$ ) for the purpose of comparison with the finite resistivity  $\eta_s V_A^2=1.6$  plots of subplots (b) and (d), respectively. The other parameters are the same as that of Fig. 1.

from zero even before  $k_z=k_{zc}$  to finally asymptote towards the drift  $k_y V_n/(1+k_\perp^2)$  and the shear-Alfvén branch  $-k_z V_A$  at large enough  $k_z V_A$ . The growth rate too unlike the case of  $\eta_s=0$  continues to remain finite even for  $k_z > k_{zc}$ , i.e., the unstable domain of the  $k_z$  space gets widened. This happens essentially because of the presence of resistivity driven modes; viz., the resistive “g” and the resistive drift mode. The expenditure of energy in causing the field line bending along the parallel direction (for  $\omega/k_z v_{the} > 1$  modes) leads to the stabilization of the RT instability for finite  $k_z$ . The field lines bend due to the parallel component of the current. In the presence of resistivity the parallel currents gets damped. This leads to the recovery of instability in the resistive time scales, and is the physical basis of the excitation of the resistive interchange mode. The resistive drift wave arises in the regime  $\omega < k_z v_{the}$  where the  $n, \phi$  relation wants to be Boltzmann-like but acquired deviations because of finite resistivity effects; the phase difference between  $n$  and  $v_{ph}$  permits energy exchange between the waves and the fluid and leads to the resistive drift-wave instability.

In Fig. 3 we depict the features of resistivity driven branch in more detail. It shows the plot of real (solid lines) and imaginary (dashed lines) part of the frequency for this branch. The ideal results  $\eta_s=0$  are plotted in subplot (a) ( $V_g=0.0364$ ) and subplot (c) ( $V_g=0.01$ ) to be compared with the finite resistivity  $\eta_s V_A^2=1.6$  plots of subplots (b) and (d), respectively. As mentioned earlier a finite growth rate beyond  $k_z=k_{zc}$  is because of the two resistivity driven modes, namely, the resistive interchange mode and the resistive drift wave. The region where  $\omega_i \gg \omega_r$  has the characteristics of the resistive interchange mode; in the opposite limit  $\omega_r \gg \omega_i$  it is the resistive drift wave.<sup>20</sup> The figure also shows that as we reduce the value of  $V_g$  the resistive drift regime gets broad-

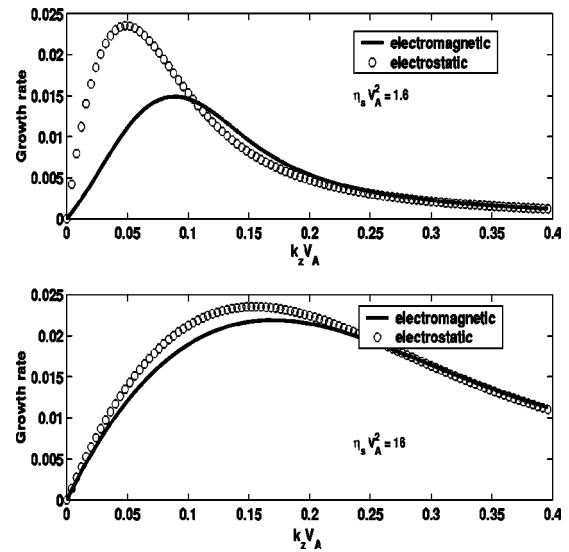


FIG. 4. The two subplots show growth rate vs  $k_z V_A$  for resistive destabilized drift wave  $V_g=0$ ; (the other parameters being  $V_n=0.8, k_x=k_y=0.1, D=\mu=0$ ) from the fully 3D electromagnetic dispersion relation of Eq. (8) (solid lines, here) and for the simplified 3D electrostatic dispersion relation of Eq. (19) (circles). The growth rates for the two models differ at small  $k_z V_A$  in the upper subplot for which resistivity parameter  $\eta_s V_A^2=1.6$ . They yield almost identical growth rates for large  $\eta_s V_A^2=16$  as shown in the lower subplot.

ened, ( $\omega_r$  asymptotes to the drift-wave frequency at a lower  $k_z$ ).

In Fig. 4 we have isolated the growth rate of the resistive drift mode by choosing  $V_g=0$ . One can see from the plots that the growth rate due to this mode vanishes for  $k_z=0$ . An analytical expression for the growth rate of this particular mode can be obtained perturbatively in the small  $\eta_s$  limit as we show below. We look at the dispersion relation of Eq. (8) in the limit of finite  $\eta_s$ . We put  $D=\mu=0$  for simplification. The dispersion relation in this case is similar to Eq. (9) but with an additional  $\eta_s$  dependent term, which is responsible for instability,

$$(\omega - k_y V_n + i \eta_s k_\perp^2 V_A^2) \left\{ \omega^2 - k_y V_g \omega + \frac{k_y^2}{k_\perp^2} V_g (V_n - V_g) \right\} = k_z^2 V_A^2 (1 + k_\perp^2) \left\{ \omega + \frac{k_y (V_g - V_n)}{(1 + k_\perp^2)} \right\}. \quad (15)$$

The effect of  $\eta_s$  on the drift wave can be seen by taking the limit  $V_A^2 \rightarrow \infty$  and  $V_g=0$  in Eq. (15),

$$\omega - \frac{k_y V_n}{(1 + k_\perp^2)} = i \frac{\eta_s k_\perp^2}{k_z^2 (1 + k_\perp^2)} \omega^2. \quad (16)$$

Considering the term on right-hand side as a small correction (possible when  $\eta_s$  is small and  $k_z$  is large) the dependence of  $\eta_s$  on  $\omega$  can be obtained iteratively as

$$\omega = \frac{k_y V_n}{(1 + k_\perp^2)} + i \frac{\eta_s k_\perp^2}{k_z^2} \frac{k_y^2 V_n^2}{(1 + k_\perp^2)^3}, \quad (17)$$

which shows the resistive destabilization of the drift-wave branch. The expression obtained above shows that the growth rate reduces as  $k_z$  is increased. The small  $k_z$  limit can

be captured by ignoring  $\omega$  in the quadratic dispersion relation of Eq. (16) giving

$$\omega = k_z \left( \frac{k_y V_n}{\eta_s k_\perp^2} \right)^{1/2} \frac{1+i}{\sqrt{2}}. \quad (18)$$

This shows that the growth rate increases with  $k_z$  indicating  $\gamma$  vs  $k_z$  must pass through a maximum, as seen in Fig. 4.

We next look at the linear properties of the simplified three-dimensional electrostatic model equations [Eqs. (5) and (6)]. This model basically contains the Rayleigh–Taylor mode and the drift-wave mode, but the coupling to the shear-Alfvén branch is absent. The dispersion relation for this set is

$$\begin{aligned} \omega^2 + \omega \left\{ -k_y V_g + i \frac{k_z^2}{\eta_s} \frac{1+k^2}{k^2} \right\} + \frac{k_y^2}{k^2} V_g (V_n - V_g) \\ - i \frac{k_y k_z^2}{\eta_s k^2} (V_n - V_g) = 0. \end{aligned} \quad (19)$$

Clearly, one recovers the two-dimensional RT growth rate expression in the  $k_z^2=0$  or  $\eta_s \rightarrow \infty$  limit. The first-order perturbative corrections show damping due to  $\eta_s$  and add a perturbative correction to the real frequency of this mode. The drift-wave dispersion relation can also be recovered provided  $k_z$  is finite. Taking  $V_g=0$  and considering  $\eta_s$  to be small the dominant balance is between the two  $k_z^2$  dependent terms in Eq. (19) from which we obtain the standard drift-wave dispersion relation of  $\omega = k_y V_n / (1+k^2)$ . Retaining the first-order correction due to the remaining  $\eta_s$  dependent term we obtain the same expression for the resistive destabilization as that of Eq. (17).

The role of  $\eta_s$  on the drift-wave branch for the general nonperturbative case can be gleaned from the plot of Fig. 4 for both the electromagnetic and the simplified electrostatic models. The upper subplot for  $\eta_s V_A^2 = 1.6$  clearly shows that the two growth rates obtained from the two models differ at small  $k_z V_A$  but agree well at large values of  $k_z V_A$ . At small  $k_z V_A$  the growth rate obtained from the fully electromagnetic dispersion relation is found to be smaller than the electrostatic case, which basically shows that the addition of electromagnetic effects cause stabilization. The two growth rates, however, show a similar trend in both cases, namely, they first increase with  $k_z$  and reach a maximum value and then fall off with  $k_z$ . The decreasing trend with  $k_z$  is captured by the perturbative expression of Eq. (17), which is valid when  $\eta_s/k_z^2$  is small. Furthermore, the lower subplot of the figure also shows that for large values of  $\eta_s V_A^2 (=16)$  the agreement between the two models is excellent over the entire range of  $k_z V_A$ . This is a further evidence of the fact that the approximations used in the derivation of the simplified electrostatic model are very accurate in the limit of large resistivity. Though the other two modes are essentially damped by the finite value of  $\eta_s$ , the resistive destabilization of the drift mode can enhance the growth rate of the coupled system.

To summarize, linear analysis of the system shows that inclusion of the third dimension introduces additional unstable modes and the presence of electromagnetic effects brings about a coupling to shear-Alfvén modes. It is then of interest to understand the nonlinear evolution characteristics

of these modes and their evolution into possible saturated nonlinear states. The simplified electrostatic model can be useful in isolating the physics due to finite  $k_z$  (parallel variation) from the electromagnetic characteristics. In the next two sections we present the nonlinear evolution studies of these two models with the help of numerical simulations.

#### IV. NONLINEAR SIMULATION RESULTS FOR THE 3D ELECTROSTATIC MODEL

We begin by presenting and discussing the results of numerical simulation studies of the simplified 3D electrostatic model represented by Eqs. (5) and (6). The equations are evolved with the help of a fully dealiased pseudospectral scheme.<sup>1,2</sup> Most of the studies have been carried out with a resolution of  $64 \times 64 \times 64$  Fourier modes in the three directions. Some test studies were also carried out with a lower resolution of  $64 \times 64 \times 16$  modes.

We first investigate the question of the existence of saturated nonlinear states. In our earlier two-dimensional studies it was shown that, even in the absence of any boundary or initial condition related anisotropy, there are two distinct symmetry states to which the system goes in the nonlinear state. The system ultimately forms growing streamer structures which are radially (along  $x$  in the slab description) elongated or to poloidally ( $y$  direction) symmetric saturated zonal patterns. For a fixed value of the driving parameters  $V_n$  and  $V_g$ , the condensation to these symmetry states was governed by the value of dissipative coefficients  $D$  and  $\mu$ . We now investigate the role of three-dimensional perturbations on the development of these symmetry patterns. We choose the perpendicular box dimensions as  $L_x = L_y = 20\pi\rho_s$ , so that there is no boundary related anisotropy in the perpendicular plane.  $L_z$  is chosen as  $1.25 \times 10^5 \rho_s$ ; this is to concentrate on low frequency modes of interest which are extended along the field lines and have  $k_z/k_\perp \ll 1$ . We choose the parametric regimes close to the 2D case in order to study the effects of parallel scales  $k_z$  and the resistivity parameter  $\eta_s$  on the formation of nonlinear states. We chose  $D = \mu = 0.1$ ,  $V_n = 0.8$ ,  $V_g = 0.036$ , a parametric region that corresponds to saturated zonal patterns for the two-dimensional case and have made several simulation runs for different values of  $\eta_s$  ( $\leq 10^{-5}$ ) and starting with small amplitude random initial perturbations in  $n$  and  $\phi$ . The chosen values of  $V_n$  and  $V_g$  also correspond to those of the currentless toroidal device BETA on which several experiments on the MCD-RT have been carried out. For this machine the typical value of  $\eta_s = \nu/\omega_{ce} \sim 10^{-5}$  and the parallel scale lengths are typically of the order of  $L_z \approx 125 Mts$ . ( $L_z = 2\pi nR$  with the major radii  $R \approx 45$  cm and  $n \approx 30$ – $50$  is the observed toroidal winding number of the magnetic field lines in this machine.) Our results are applicable to other values of  $\eta_s$  and  $k_z$  through the scaling arguments described with Eq. (7) and may also be applied to the spread  $F$  region of the ionosphere, edge localized mode (ELM) region of tokamaks, etc. (for more details please see the last section).

A typical 3D representation of the initial random potential  $\phi$  structure is shown in the form of a slice plot in Fig. 5. These slice plots basically show the pattern of a particular



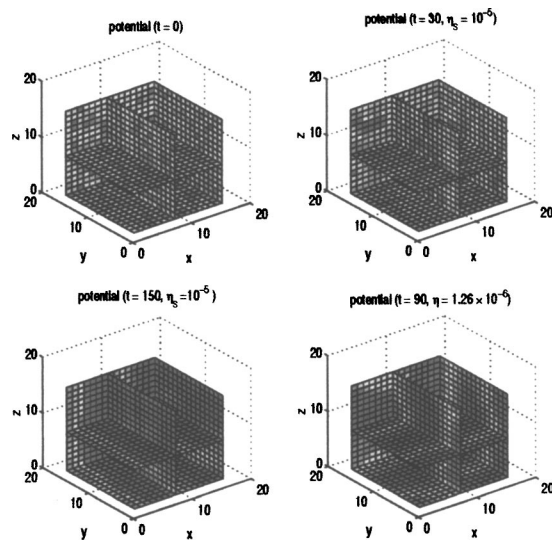


FIG. 5. (Color online). The slice plots (described in text) for potential  $\phi$  field to visualize its three-dimensional structure at various times for the 3D electrostatic evolution equations (5) and (6). The parameters for this case are  $V_n=0.8$ ,  $V_g=0.036$ ,  $D=\mu=0.1$ . The simulation box sizes are  $L_x=L_y=20\pi\rho_s$ ,  $L_z=1.25\times 10^5\rho_s$ . The first three plots (as indicated on the top) are for  $\eta_s=10^{-5}$  at  $t=0$ , 30, and 150 and show the formation of zonal  $y$  symmetric pattern in the final nonlinear state at  $t=150$ . The fourth plot corresponds to a different run for which  $\eta_s$  is  $1.26\times 10^{-6}$ , and shows formation of radially (along  $x$ ) extended streamer structure.

field variable with the help of color (in color plots) or through shading (in gray plots) on various two-dimensional slice planes of the three-dimensional space. The appropriate slicing helps in the three-dimensional visualization of the field pattern. For instance in the plot of Fig. 5 (and also in all the subsequent slice plots presented in this paper) we have chosen five different slices of the three dimensional volume of  $L_x\times L_y\times L_z$ . The different slices are the  $x$  vs  $y$  plane at  $z=0$  and  $z=L_z/2$ ;  $y$  vs  $z$  plane at  $x=L_x/2$  and  $L_x$ ; and  $x$  vs  $z$  plane at  $y=0$ .

The initial density  $n$  field has a similar structure containing many short scales in a random configuration. For the small amplitudes chosen initially the evolution is primarily governed by the linear terms. Thus, during the initial linear phase modes having maximal growth rate acquire the largest amplitudes and dominate the spectrum. Since the maximally growing modes are the RT modes that have large  $k_y$  but small  $k_x$ , we can expect to see, in the early linear stages of development, the appearance of structures which are elongated along the  $x$  direction. We see clear evidence of such structures in the slice plot for the potential at  $t=30$  in Fig. 5. As the amplitudes grow, the modes start interacting and one expects the power to get transferred to linearly stable modes as well. In the present case we see such a phenomenon too and find the power in potential  $\phi$  field nonlinearly cascading towards long scales. Such a cascade towards long scales is an intrinsic property of the polarization drift nonlinearity that is present in the evolution equation of  $\phi$ .

We have carried out simulations both for large and small resistivity parameters  $\eta_s$ , and observe distinct difference in the two regimes. For large values of  $\eta_s$ , viz.,  $10^{-5}$ , nonlinear saturated zonal symmetry patterns in potential  $\phi$  field are

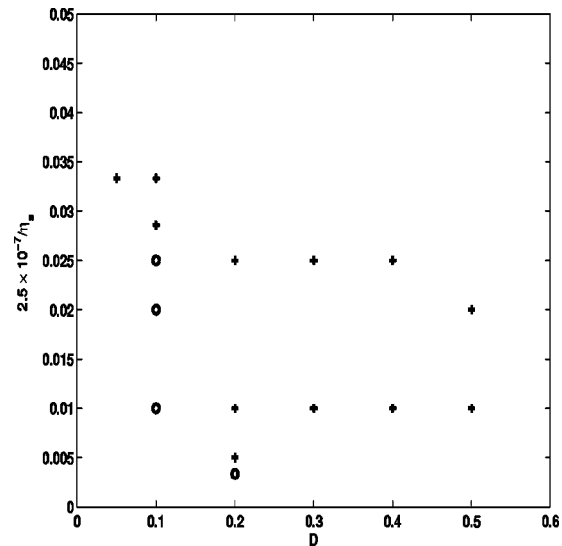


FIG. 6. The parametric regime of  $D$  vs  $1/\eta_s$  space in which the circles indicate those values of  $D$  and  $1/\eta_s$  for which nonlinear saturation was achieved. The evolution is governed by the 3D electrostatic set of equations (5) and (6). The other parameters have the same values as that chosen in Fig. 5.

seen to form (see Fig. 5). However, when  $\eta_s$  is small  $=1.26\times 10^{-6}$  there is no saturation and growing streamer patterns are observed (Fig. 5). Thus in three dimensions, as the available phase space of the modes get enhanced with the addition of finite  $k_z$  modes, the resistivity parameter  $\eta_s$  along with  $D$  and  $\mu$  determine the symmetry pattern of the potential structure in the nonlinear stage. Figure 6 shows the simulation cases in the parametric space of  $D$  vs  $1/\eta_s$  for which saturated states were achieved (by circles) and those for which only growing streamer patterns were observed by + (plus) signs. This trend is consistent with the fact that at large values of  $\eta_s$  the contribution of the additional linear and nonlinear terms arising from 3D effects become small and are negligible in comparison with other terms and the set of equations tend to reduce to the previous two-dimensional equations. This has been quantitatively illustrated in Fig. 7, which shows the plot of the ratio of growth rate  $\gamma$  with  $k_z^2/\eta_s$  as a function of  $k_z$  yielding saturated zonal (by circles) and growing streamers (+ sign) for  $\eta_s=10^{-5}$  and  $\eta_s=1.26\times 10^{-6}$ , respectively. The range of  $k_z$  shows the permissible parallel wave numbers of the simulation after aliasing. It is clear from the plot that when  $\eta_s=1.26\times 10^{-6}$ , there are parallel scales for which the ratio drops below unity (signifying the dominance of the extra three-dimensional terms in the evolution equation and consequently the dynamics being altered significantly). On the other hand for large values of  $\eta_s=10^{-5}$  there are no parallel scales for which the additional terms dominate, the dynamics thus is close to the previous two-dimensional scenario for which saturated structures were obtained.

However, there are a few interesting differences in the composition of the final saturated state for the two- and three-dimensional cases even though the additional terms are merely small perturbative corrections for such numerical runs. In the two-dimensional simulations the density field

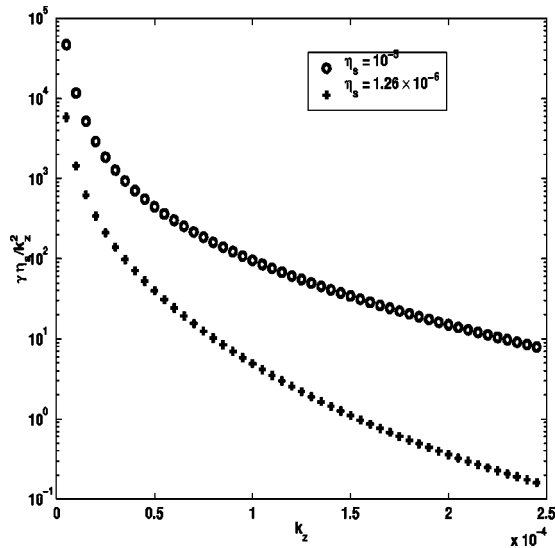


FIG. 7. Plot of the ratio  $\gamma\eta_s/k_z^2$  vs the permissible range of  $k_z$  in simulation. The two plots are for  $\eta_s = 1.26 \times 10^{-6}$  (+ sign) which corresponds to unsaturated streamers and  $\eta_s = 10^{-5}$  (circles) which yields saturated zonal structures in the nonlinear simulation.

was observed to get slaved to  $\varphi$  and it too displayed the formation of long scale structures with two distinct symmetries. For the three-dimensional runs, however, we see, from the plot of Fig. 8, that the density field continues to be dominated by power in the short scales. The scatter plots between the density and the potential fields (see Fig. 9) also does not show any evidence of functional relationships developing between density and potential fields. The vorticity  $\nabla^2\varphi$  too, unlike the previous case, has significant power in short scales (Fig. 8) and does not form any functional relationship with the potential  $\varphi$  field (see Fig. 9).

The nonslaving of the density field can be understood by realizing that due to parallel variations, additional modes

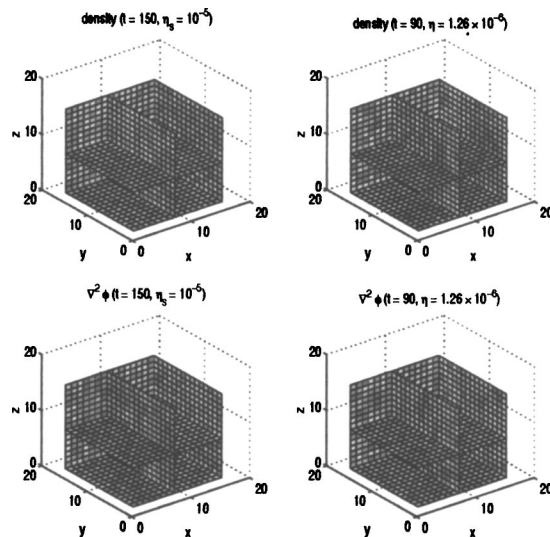


FIG. 8. (Color online). The slice plots for density and vorticity  $\nabla^2\phi$  in the nonlinear state for two different values of  $\eta_s$  (viz.,  $10^{-5}$  and  $1.26 \times 10^{-6}$ ). The other parameters and the governing evolution equation are same as that of Fig. 5.

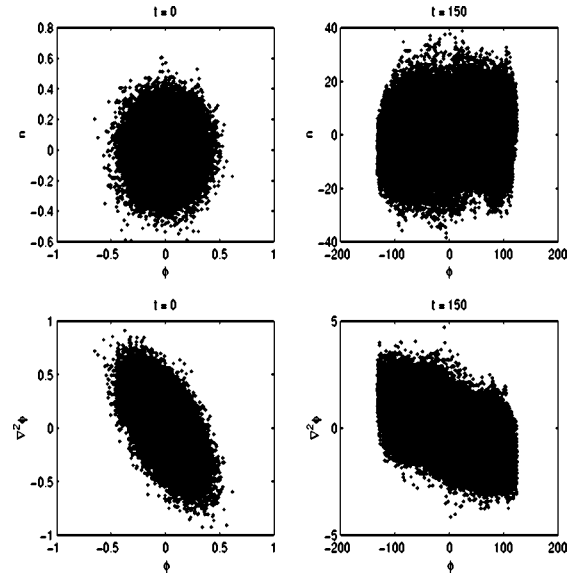


FIG. 9. Scatter plots between  $n$  and  $\varphi$  and between  $\nabla^2\varphi$  and  $\varphi$  initially at  $t=0$  and at the stage where saturation is achieved at  $t=150$ . The data for  $n$  and  $\varphi$  are the same as that of Fig. 5 with  $\eta_s = 10^{-5}$ . Clearly, the plots show no development of any kind of functional relationship unlike the 2D case (Ref. 2).

(drift waves, etc.) having very different linear mode relationship amidst the two fields compared to the RT modes get excited (e.g., typically  $n_k \sim \varphi_k$  for drift waves, whereas for RT mode the density and potential fields are essentially out of phase). This may hinder the slaving process of density to the potential. Moreover, two-dimensional set of equations conserve the following nondissipative integral invariant:

$$\iint \left\{ (\nabla\varphi)^2 - \frac{V_g}{(V_n - V_g)} n^2 \right\} d^2r = \text{const}, \quad (20)$$

which clearly shows an establishment of integral relationship between the density and the potential fields. Such a integral relationship is consistent with the possibility of the  $n$  field getting slaved to  $\varphi$ . The incorporation of 3D effects, however, rules out any integral constraint on the two fields. We have in this case instead,

$$\begin{aligned} & \frac{1}{2} \frac{\partial}{\partial t} \iiint \left\{ (\nabla\varphi)^2 - \frac{V_g}{(V_n - V_g)} n^2 \right\} d^3r \\ &= - \frac{1}{\eta_s} \iiint \left\{ \left( \varphi + \frac{V_g n}{(V_n - V_g)} \right) \frac{\partial^2}{\partial z^2} (n - \varphi) \right\} d^3r. \end{aligned} \quad (21)$$

The dissipation parameter  $\eta_s$  has been retained, as the 3D effects here arise solely from  $\eta_s$  dependent term. Clearly, since the two fields do not satisfy any integral relationship in the 3D case, it is not easy for the density field to get slaved to  $\varphi$ . It thus seems that the nonexistence of any integral constraint and the absence of any functional relationship between  $n$  and  $\varphi$  along with the fact that the nonlinear evolution of the density field is governed directly by the convective nonlinearity, viz.,  $\hat{z} \times \nabla\varphi \cdot \nabla n$  which cascades power towards short scales, leads to the predominance of power in short scale fluctuations in  $n$ . The polarization nonlinearity

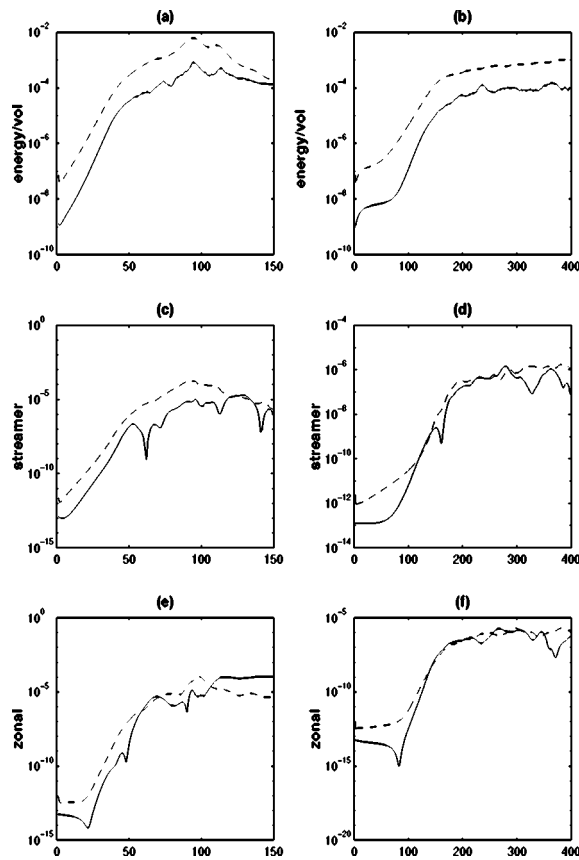


FIG. 10. The numerical evolution of energy, streamer, and zonal intensity per unit volume with time for the 3D electrostatic model of Eqs. (5) and (6); for the Rayleigh–Taylor (subplots in left column) and the resistive drift mode (subplots in the right column) for comparison. The plots in solid lines show the intensity in  $k_z=0$  modes and the dashed lines indicate the power in finite  $k_z$  modes.

influences the  $n$  evolution only indirectly through  $\varphi$ .

It should be noted that in the above runs with finite  $\eta_s$ , the linear phase has two unstable modes—the RT mode and the drift mode which is made unstable by the resistivity. In order to understand the role of the unstable drift wave it is possible to isolate its behavior by artificially turning off the RT mode. We have carried out such an investigation by setting  $V_g=0$  and looking at the nonlinear evolution of the drift modes. The value of the resistivity parameter was chosen to be  $\eta_s=10^{-5}$ . Figure 10 shows a comparison of the growth and evolution of the total energy, the zonal, and streamer powers for RT mode and the resistive drift wave. The slower linear rise can be understood from the lower growth rate of the resistivity driven drift wave in comparison to the growth rate of the RT mode. It is interesting to observe that in the final saturated regime of the resistive drift case, there is no dominance of power in the zonal mode as observed in the context of RT. This leads to a characteristic mixed flow pattern in which one cannot clearly distinguish between the zonal and streamer symmetries. Such a saturated state of the potential fluctuation at  $t=450$  is shown as a slice plot in Fig. 11. It is also interesting to observe that for the resistive drift wave the energy level in finite  $k_z$  modes is an order of magnitude higher than that in the  $k_z=0$  modes.

In all of the above simulations we have avoided intro-

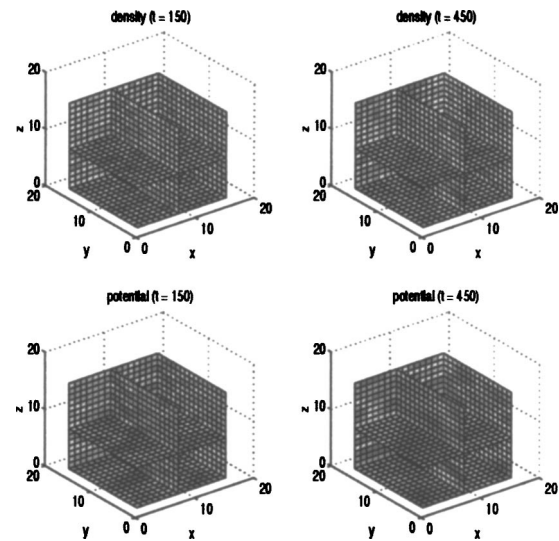


FIG. 11. (Color online). Slice plots showing the three-dimensional density and potential structures in the linear ( $t=150$ ) and the nonlinear ( $t=450$ ) regimes for the resistively destabilized drift waves.

ducing any perpendicular anisotropy associated with boundary and initial conditions. We restricted ourselves to those simulations for which the perpendicular aspect ratio of the simulation box was unity, i.e.,  $L_x=L_y$ . The simulation volume  $L_x \times L_y \times L_z$  basically represents a small region of the entire plasma. By simulating over a small region one hopes to identify and understand the basic features of turbulent excitations. The simulation, however, gets constrained by the choice of box sizes in a few ways; the longest scale length along a particular direction is determined by the box length along that direction. In some cases as we would show below, a natural process of power cascade towards a long scale asymmetric mode can get inhibited by a certain choice of the aspect ratio of the simulation box size. The unlimited growth of streamers observed by us earlier for the choice of aspect ratio unity is one such example. It is well known that a shear flow excites Kelvin–Helmoltz (KH) instability; however, in our simulations carried out with  $L_x=L_y$  we observe no development of secondary KH instability which could prevent the unlimited growth of streamers in the parameter domain indicated by the + sign of the plot in Fig. 6. This happens because the essential condition for the excitation of KH instability on streamer shear flow (with shear scale length of  $L_y$ ) can never be met within the restriction of square box size. The KH instability can be excited only when the perturbation scales (in the orthogonal direction) are longer than the background shear scale length. With  $L_x=L_y$  there can be no such mode to support such a secondary destabilization process of streamers. By relaxing the constraint of  $L_x=L_y$ , and choosing instead  $L_x>L_y$  (we chose  $L_x=4L_y$ ) we observe that the unlimited and unphysical growth of streamers is prevented. In Fig. 12 we show a comparison of the evolution of total energy  $\iint [n^2 + (\nabla\varphi)^2] dx dy$  for the two cases, viz.,  $L_x=L_y$  (solid lines) and  $L_x=4L_y$  (dotted lines). The other parameters for the two cases are identical. The plot clearly shows that when the box dimensions are identical the energy grows indefinitely and there is no saturation. On

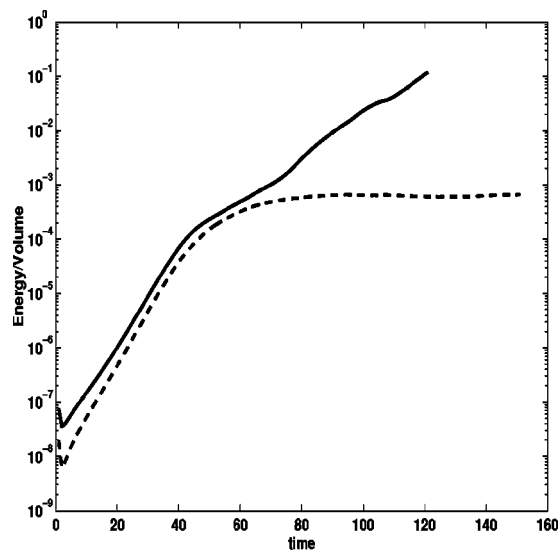


FIG. 12. The evolution of total energy/volume for the case when  $L_x/L_y=1$  (solid line) and when  $L_x/L_y=4$ .

the other hand when  $L_x$  is chosen to be longer than  $L_y$  the energy saturates. This has important implications on transport. It shows clearly that simulations with those parameters which require  $L_x > L_y$  for saturation; excites flows with radial scale length longer than the ones for which the instability saturates for  $L_x = L_y$ . Since the radial decorrelation step size is essentially determined by the radial scale length of the structures, it implies that the transport will be high for the parametric regime (+ sign of Fig. 6) which do not saturate for a square box size (aspect ratio unity).

To summarize, in this section we have shown that similar to the 2D simulations the 3D electrostatic model too is capable of supporting nonlinear saturated states that are dominated by long scale zonal flow patterns. Here too, even in the absence of any boundary or initial condition related bias, the nonlinear evolution lead to the condensation towards either saturated zonal flow patterns or growing streamer formations depending on the strength of the various dissipation parameters. The model has an additional dissipation parameter in the resistivity coefficient which plays a special and distinctly different role than the other two dissipation parameters in the selection of the final stage. The density field in the 3D saturated cases show distinct features of short scale dominance and non slaving to the  $\varphi$  field; which is distinctly different from the 2D results. Furthermore, the resistivity parameter also leads to the excitation of additional instabilities, e.g., resistive interchange and the resistive drift waves. Simulation studies on the unstable resistive drift wave were also carried out which show new variety of nonlinear state in which zonal and streamer powers were comparable. It was also shown that the parameter regimes for which one obtains unsaturated streamer patterns could be stabilized by increasing the aspect ratio  $L_x/L_y$  from unity. This basically enables the secondary KH destabilization of the streamer patterns. It was shown that such cases would be responsible for higher transport.

## V. SIMULATION OF THE 3D ELECTROMAGNETIC MODEL

We now turn to the generalized three-dimensional model represented by Eqs. (1)–(3) and discuss its numerical solutions. In comparison to the 3D electrostatic case we now have an additional field variable  $\psi$  (the magnetic vector potential), whose temporal evolution is governed by Eq. (3) and which provides additional coupling (linear and nonlinear both) terms in the evolution equations of the density and potential variables. The coupling coefficient is proportional to  $V_A^2$  (i.e., inversely proportional to  $\beta$ ) as well as to the spatial variation in the parallel direction (i.e., to  $k_{||}$ ). As mentioned before the influence of electromagnetic effects will be felt when  $\partial\psi/\partial t$  becomes comparable to  $\eta_s V_A^2 \nabla^2 \psi$ . The order of typical perpendicular wavenumbers ranging from 0.1 to unity for our simulations, it implies a direct comparison of  $\eta_s V_A^2$  with the growth rate. When  $\eta_s V_A^2 \gg \gamma$ ,  $\psi$  is essentially damped, electromagnetic effects are weak and energy in the magnetic field is typically small. This is the limit where the generalized 3D electromagnetic model is expected to reduce to the 3D electrostatic model discussed in detail in the last section. The parameter regime of  $\eta_s V_A^2 \ll \gamma$  to  $\eta_s V_A^2$  of the order of  $\gamma$  is thus of interest for studying the influence of electromagnetic effects on the dynamics.

In this section we present results for the case of  $\eta_s V_A^2 = 1$ . For this value of  $\eta_s V_A^2$  we expect the electromagnetic effects to become significant enough so as to influence the dynamics. Furthermore, this choice is also motivated by the fact that it is the parameter regime relevant for the currentless toroidal BETA machine at Institute for Plasma Research (IPR). A detailed parametric simulation study for  $\eta_s V_A^2$  ranging from  $\ll \gamma$  to  $\gg \gamma$  for the 3D electromagnetic set of equations are, however, underway and will be presented elsewhere.

We look for saturated states in a square box geometry with ( $L_x = L_y$ ). The other parameters are  $V_g = 0.036$ ,  $V_n = 0.8$ ,  $D = \mu = 0.1$ , and  $2\pi V_A/L_z = 10^{-3}$ . The plot in Fig. 13 shows the evolution of the total and the magnetic energy (solid and dashed lines, respectively). The energy is seen to saturate after an initial exponential growth. The saturated magnetic energy is an order of magnitude smaller than the total energy for this set of parameter values. Thus the electromagnetic fluctuations are not dominant in this particular simulation. However, we present a comparison with the electrostatic case to show that even in this case, though the amplitude of electromagnetic fluctuations are low, their effect on the nonlinear saturated state is significant. The linear growth of energy for both electromagnetic and electrostatic cases are similar. This is because the value of the maximum growth rate in both the cases are identical. However, in the nonlinear regime the electrostatic total energy is smaller due to a mild decay during the later phase. The lower subplot of the same figure shows the evolution of intensity of zonal and the streamer modes. The zonal intensity for both electrostatic and the electromagnetic cases are at identical level. The intensity of the streamer mode, however, in the electrostatic case is considerably smaller and exhibits a mild decay similar to what is observed for the total energy. It is interesting to



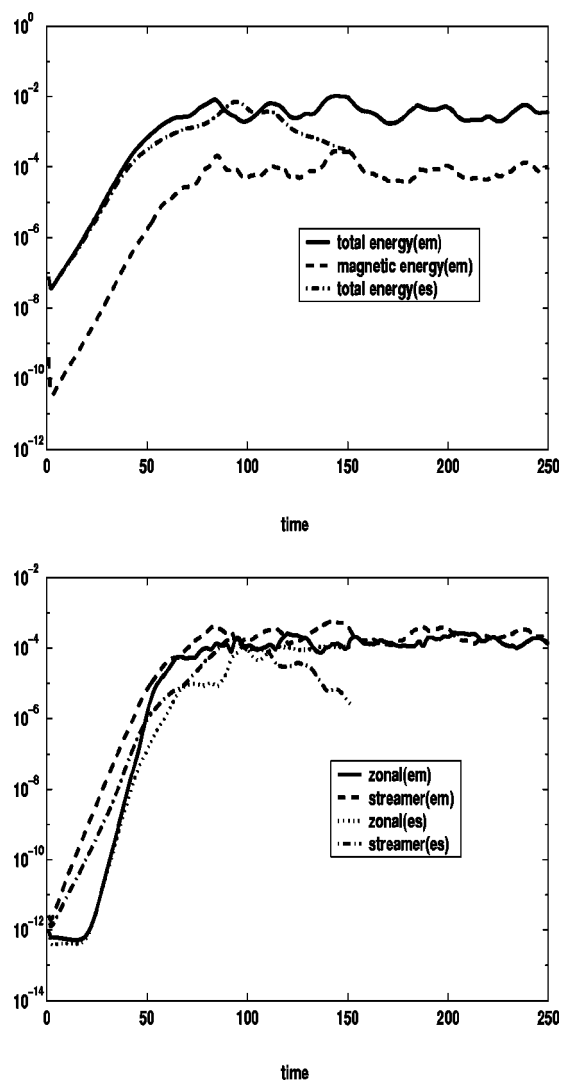


FIG. 13. The upper subplot shows the evolution of kinetic (solid line), pressure (dashed line), and the magnetic (dotted line) energy for the fully generalized electromagnetic simulations of Eqs. (1)–(3). The lower subplot shows evolution of power in zonal (solid line) and streamer modes (dashed line).

note that in the electrostatic case even though the total energy in turbulent fluctuations are small compared to the electromagnetic case, the zonal intensity is identical, i.e., as a relative fraction, zonal flow intensity is stronger in the electrostatic case. This clearly implies that it is much easier to generate zonal flows in the electrostatic case, confirming the prevalent lore that that electromagnetic effects inhibit the zonal flow generation. The streamer intensity in electromagnetic case being higher also confirms that the stabilization of the instability in the presence of electromagnetic effects becomes difficult.

In Fig. 14 we depict the slice plots for the three fields, viz.,  $n$ ,  $\phi$ , and  $\psi$  in both the linear as well as the nonlinear regimes. In both linear and nonlinear regimes we observe considerable structure in all the three fields in the  $z$  direction, indicating that energy in the finite  $k_z$  modes are significant. Unlike the clear symmetry breaking nonlinear stages (growing streamers or saturated zonal depending on the parameter regimes in the  $D$ ,  $\mu$ , and  $\eta_s$  space) of the 3D electrostatic RT

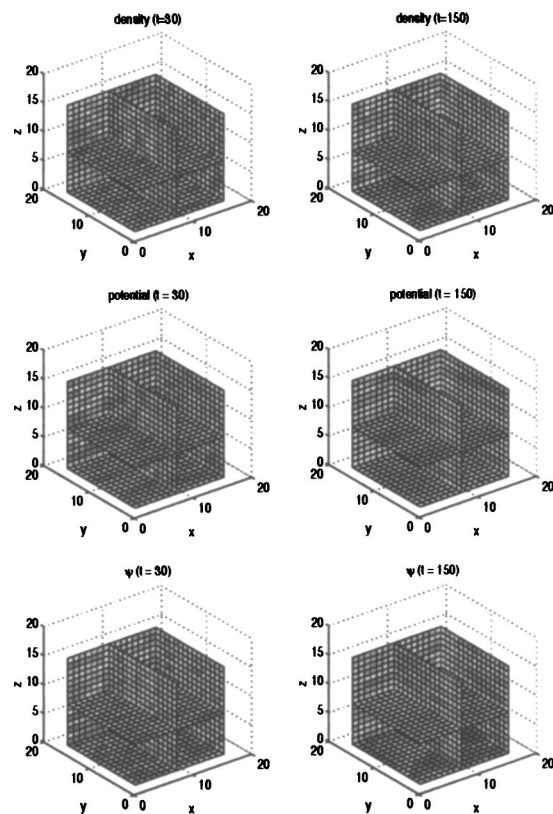


FIG. 14. (Color online). The slice plots showing three-dimensional patterns for  $n$ ,  $\phi$ , and  $\psi$  in the linear  $t=30$  and the nonlinear  $t=150$  regimes for the electro magnetic simulation corresponding to the saturated state ( $\eta_s V_A^2=1$ ) of Fig. 13.

modes, in the electromagnetic case the flow structures cannot be distinctly classified in zonal and streamer patterns. This is also evident from the evolution of zonal and streamer intensities in the plot of Fig. 13. Furthermore, the  $n$  and  $\psi$  fields show a predominance of short structures in comparison to the potential  $\phi$  field.

Our simulations also show that similar to 3D electrostatic case, here too the density remains an independent field throughout the evolution and does not get slaved to the potential field. In the 3D electrostatic context, this was attributed to the the presence of a variety of additional modes arising by permitting the three-dimensional variation in the system and also to the loss of integral invariant for the 3D equations. In the electromagnetic case where there is an increase in the variety of linear modes, (shown in detail in the third section) it is even more difficult for the two fields to develop any functional relationships.

The electromagnetic studies of this section reveal that the features, which were earlier (with the help of electrostatic studies), attributed to the three dimensionality of the system are present in these simulations also, the sytem being three dimensional here as well. However, additionally we observe that even the presence of a weak electromagnetic energy considerably opposes the process of nonlinear stabilization.

## VI. SUMMARY AND CONCLUSIONS

In this work we have studied the extension of a previous two-dimensional nonlinear model evolution equations<sup>1,2</sup> for the magnetic-curvature-driven Rayleigh–Taylor instability to

three-dimensional perturbations. The extended model also incorporates coupling to electromagnetic fluctuations associated with the magnetic field line bending terms through the parallel component of the Ohm's law. The objective of the present work has been to investigate the influence of three dimensionality and the electromagnetic effects on the nonlinear state. It was shown that the effects due to three dimensionality can be isolated by considering a simplified 3D electrostatic limit. Such a limit is valid when the typical growth rates are much smaller than the parameter  $\eta_s k_\perp^2 V_A^2$ . Here  $\eta_s$  is the resistivity parameter defined earlier in the text,  $\beta = 1/V_A^2$  represents the plasma beta, and  $k_\perp$ , the typical perpendicular scales.

Studies on 3D electrostatic model show that the  $D$ - $\mu$  phase space, which in earlier 2D studies<sup>1</sup> governed the symmetry of nonlinear flow patterns (viz., the transport inhibiting saturated zonal flows versus the transport enhancing growing streamers) gets extended by the inclusion of a third dissipative parameter, viz.,  $\eta_s$ . A comprehensive parametric study reveals that the resistivity parameter, has an entirely different role in pattern selection process. While smaller values of both  $D$  and  $\mu$  form zonals and their larger values streamers, it is the opposite for  $\eta_s$ . In 2D simulations it was observed that the density field ultimately develops a functional relationship with potential. The power cascade towards long scale for the potential in 2D case ultimately also forces the density to acquire long scale structures. It was observed in our current 3D simulations that the density was not in any way constrained to follow the potential field. Hence, in the 3D case the density field continues to have power in short scale fluctuations. Another feature of the 3D model, in contrast to 2D, is the existence of additional resistivity driven modes. Nonlinear studies on resistively destabilized drift wave (with RT growth switched off) yielded a novel variety of saturated states which have neither zonal nor streamer symmetries; instead the intensities of both zonal and streamer flows were at comparable level.

The electromagnetic effects on RT were studied by simulating the fully 3D electromagnetic set of equations. At the moment we have carried out investigations only for those parameters for which the electromagnetic effects are weak and the magnetic energy is an order of magnitude smaller than the total energy. This was achieved by choosing  $\eta_s V_A^2 = 1$ , which is still larger than the maximum growth rate  $\gamma_{\max} = 0.16$ . These simulations clearly show that even though the electromagnetic energy is weak, its presence inhibits the zonal formation leading to a relatively higher amplitude of streamers. Thus, as expected, the presence of electromagnetic effects hinders the saturation process.

Curvature or gravity driven RT modes are important in many magnetized plasma problems. They were extensively studied experimentally in the toroidal currentless plasma machine BETA.<sup>21</sup> As stated in the text, the parameters of BETA were such ( $V_n = 0.8$ ,  $V_g = 0.036$ ,  $L_z = 1.25 \times 10^5 \rho_s$ ,  $\eta_s \sim 10^{-5}$ ) that the results of present study are directly applicable. In the context of tokamaks, curvature-driven ballooning modes (with or without resistivity effects) are relevant to the core region, as well as the edge region (especially when the plasma exhibits the edge localized modes called ELMS). The

typical parameters in the core region are ( $\eta_s \sim 10^{-7}$ ,  $V_A^2 = 1/\beta = 10$ , implying that  $\eta_s V_A^2 \sim 10^{-6}$ ,  $L_z/\rho_s = 2\pi qR/\rho_s = 2 \times 10^4$ ,  $V_n = \rho_s/L_n \approx 0.1$ , and  $V_g = \rho_s/R \approx 10^{-2}$ ) and those in the edge region are ( $\eta_s \sim 2.5 \times 10^{-5}$ ,  $V_A^2 = 1/\beta = 10^3 - 10^4$ , so that  $\eta_s V_A^2 \sim 1$ ,  $L_z/\rho_s = 2\pi qR/\rho_s = 2 \times 10^4$ ,  $V_n = \rho_s/L_n \approx 0.1$ , and  $V_g = \rho_s/R \approx 10^{-3}$ ). Thus the present study may be applicable to the tokamak edge problem, although the driving instability in the simulations is somewhat stronger because of the higher value chosen for  $V_n$ . Gravity driven RT modes are also relevant to the spread  $F$  region of the ionosphere. The typical parameters in this region are ( $\eta_s = 10^{-5}$ ,  $V_A^2 = 1/\beta \approx 10^6$ ,  $\eta_s V_A^2 \sim 10$ ,  $L_z/\rho_s = 10^5$ ,  $v_n = \rho_s/L_n \approx 2.5 \times 10^{-3}$ , and  $V_g = 10^{-4}$ ). Thus the results of our studies are applicable to this problem also.

It should be pointed out here that several three-dimensional numerical studies on the electrostatic<sup>22,23</sup> and electromagnetic<sup>24,25</sup> nonlinear equations describing the coupling of drift ballooning modes have been carried out in the last decade or so. Such studies have employed a realistic three dimensional model for tokamaks with effects due to magnetic shear and parallel flows. These studies contain extensive details of simulation studies on transport in tokamaks. Our objective in contrast has been to delineate the parameter regime for the formation of transport inhibiting and transport enhancing structures and identification of the rudimentary physics with the choice of a simplified model (that of drift-RT coupling, in the absence of both parallel flow and magnetic shear).

Finally, we make some remarks on the further exploration of the present work that we are currently pursuing. The complete parametric study for the fully 3D electromagnetic case has not been presented here. Future studies will explore other regions of parameter space (especially lower values of  $\eta_s V_A^2$  where electromagnetic effects become more important). Thus future investigations will be carried out to understand the nonlinear stabilization process by the zonal flow formation as the parameters  $\eta_s V_A^2$  and  $\beta = 1/V_A^2$  are varied. We also want to include the finite  $T_i$  effects, because finite ion Larmor radius stabilization is an important linear mechanism of the stabilization of the curvature-driven instabilities.

## ACKNOWLEDGMENTS

The authors are thankful to Xavier Garbet and other organizers of the workshop on "Relaxations in magnetized plasmas, 7–25 July 2003" held at Aix-en-Provence, France, where part of this work was carried out.

## APPENDIX: DERIVATION OF THE GOVERNING EQUATIONS

We consider a cylindrical shell region (as shown in the schematic of Fig. 15) with the coordinate system  $R$ ,  $\theta$ , and  $Z$ , and with  $e_R$ ,  $e_\theta$ , and  $e_Z$  as unit vectors along them. The plasma density is considered to be finite in a region  $R_1 < R < R_2$  ( $R_1$  and  $R_2$  being the inner and outer radii of the cylindrical shell),  $0 < \theta \leq 2\pi$ , and  $-\infty < Z < \infty$  for the purpose of illustration. (Note choosing a limited region of  $Z$  would yield a toroidal configuration.) The width of the shell  $|R_1 - R_2| = a$  is considered to be much smaller than  $R$  itself, and terms

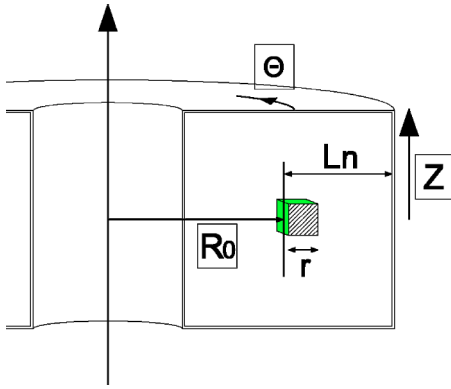


FIG. 15. A schematic diagram showing the cylindrical coordinate configuration  $R, \theta, Z$  adopted for the derivation of the governing equations in the appendix. The small shaded box represents the region of interest for which the standard slab transformation is applied.

only up to order  $\epsilon = a/R$  would be retained. The region of interest for the present work is even smaller and has been depicted by the shaded small box shown in Fig. 15 for which  $R, \theta, Z$  coordinate system would be later transformed to the slab  $x, y, z$  system adopted in the manuscript.

Let there be an external current outside the plasma region which produces a vacuum magnetic field of the form

$$\vec{B}_{vac} = \frac{B_0 R_0 e_\theta}{R}. \quad (A1)$$

(Here  $R = R_0 + r$ , since  $r/R_0$  is of order  $\epsilon$ ; we will retain terms up to order  $r/R_0$  only in the derivation of our governing equations. Since it is a vacuum magnetic field its curl is zero in the region of interest. Note that the inhomogeneity of the magnetic field arises in this case due to its “curvature.” In the absence of any curvature the magnetic field inhomogeneity would have led to a finite value of curl, thereby necessitating a current to sustain it. This is the reason why we have used the terminology, “magnetic-curvature-driven RT instability.” The slab representation has been adopted only later, the terms retained in such an approximation are consistent with the ordering scheme.

Consider the region  $R_0$  to  $R_2$  as the outboard region in which the equilibrium density profile falls off as

$$n_0(R) = n_{00} \exp(-r/L_n) \quad (A2)$$

It should be noted here that the density scale length  $L_n$  is typically of the order of  $a$  and is an order of magnitude smaller than the typical value of the magnetic field curvature, viz.,  $R_0$ . However,  $r/L_n$  is also considered to be much less than unity and only first-order terms are retained in  $r/L_n$  as well. In equilibrium, only the electron diamagnetic drift  $\vec{v}_{e0} = (c/en_0 B_{eq}^2) \nabla p_e \times \vec{B}_{eq}$  is present giving rise to an equilibrium plasma current  $\vec{J}_{eq} = -en_0 \vec{v}_{e0}$ . Let us represent the magnetic field due to this plasma current by  $\vec{B}_{p0}$ . Thus the equilibrium magnetic field is  $\vec{B}_{eq} = \vec{B}_{vac} + \vec{B}_{p0}$ .

We define  $\beta = 4\pi T_e n_{00} / B_0^2 = c_s^2 / V_a^2$ , which is a small quantity compared to unity; it is easy to show upon integration of the expression  $\nabla \times \vec{B}_{p0} = 4\pi \vec{J}_{p0} / c$  that up to  $O(\beta)$  and

keeping only the first-order terms in  $r/L_n$  and  $r/R_0$  we have  $\vec{B}_{p0}/B_0 = -e_\theta \beta (1 - r/R_0 - r/L_n)$ . Thus the magnetic field generation due to the plasma diamagnetic current are an order  $\beta$  smaller than the vacuum magnetic field. The equilibrium magnetic field can then be written as

$$\frac{\vec{B}_{eq}}{B_0} = e_\theta \left[ (1 - \beta) \left( 1 - \frac{r}{R_0} \right) + \beta \frac{r}{L_n} \right]. \quad (A3)$$

Thus the homogeneous part of the equilibrium magnetic field is dominated by the vacuum magnetic field. Even otherwise if one desires to retain the contribution due to plasma current the factor  $(1 - \beta)$  can be absorbed in normalization. The inhomogeneity due to diamagnetic effects can become comparable to the inhomogeneity of the vacuum magnetic field provided  $\beta R_0 / L_n \sim O(1)$ . Even if this particular term were retained it would merely alter the definition of  $V_g$ . We have in the manuscript considered this term to be smaller and have ignored all terms in the expression of magnetic field which are proportional to  $\beta$ . Under this approximation the equilibrium magnetic field is

$$\frac{\vec{B}_{eq}}{B_0} = e_\theta \left( 1 - \frac{r}{R_0} \right). \quad (A4)$$

For the derivation of our model we assume the following ordering:

$$\frac{\omega}{\omega_{ci}} \sim \phi \sim n \sim \frac{\psi}{\sqrt{\beta}} \sim \frac{a_s}{L_n} \sim \frac{a_s}{R_0} \sim \frac{a_s}{l_\parallel} \sim O(\delta).$$

Here  $\phi$ ,  $n$ , and  $\psi$  are the normalized perturbed fields specified in the manuscript. Also  $l_\parallel^{-1} \equiv (1/R) \partial / \partial \theta$  is the typical parallel scales of the perturbed field. We retain terms only up to  $O(\delta^2)$  in our derivation.

The relevant equations are the continuity equation, electron and ion momentum equation, and the quasineutrality condition. The perpendicular electron and ion drifts up to order  $\delta^2$  are

$$\vec{v}_{e\perp} = \frac{c \vec{E} \times \vec{B}}{B^2} + \frac{c}{eNB^2} \nabla p_e \times \vec{B}, \quad (A5)$$

$$\vec{v}_{i\perp} = \frac{c \vec{E} \times \vec{B}}{B^2} + \frac{Mc^2}{eB^2} \frac{d\vec{E}_\perp}{dt}. \quad (A6)$$

The perturbed magnetic field causes the bending of the magnetic field lines. Thus the resultant unit vector parallel to the magnetic field is  $e_\parallel = e_\theta + e_\theta \times \nabla \psi / B_{eq}$  and  $\nabla_\parallel = \nabla_\parallel + e_\theta \times \nabla \psi \cdot \nabla / B_{eq}$ , here  $\nabla_\parallel = (1/R) \partial / \partial \theta$ .

The electron continuity equation is used to obtain the evolution equation for  $n$ . We will retain terms up to order  $\delta^2$  as mentioned above

$$\frac{1}{N} \frac{\partial N}{\partial t} + \frac{1}{N} \nabla_\perp \cdot (N \vec{v}_{e\perp}) + \frac{1}{N} \nabla_\parallel \cdot (N \vec{v}_{e\parallel}) = 0. \quad (A7)$$

Now  $(1/N) \partial N / \partial t = \partial n / \partial t$ , the perpendicular flux of density in Eq. (A7) is

$$\frac{1}{N} \nabla_{\perp} \cdot (N \vec{v}_{e\perp}) = \frac{c}{N} \nabla_{\perp} \cdot \left[ N \frac{e_{\theta} \times \nabla \phi}{B_{eq}} - \frac{T_e}{e B_{eq}} e_{\theta} \times \nabla N \right]. \quad (\text{A8})$$

Using vector identities and the normalizations adopted in the text it is easy to show that the perpendicular flux can be written as

$$= \left[ e_{\theta} \times \nabla \phi \cdot \nabla_{\perp} n - (V_n - V_g) \frac{\partial \phi}{\partial Z} \right] - \left[ V_g \frac{\partial n}{\partial Z} \right].$$

The last part of Eq. (A7), viz., the parallel flux of the density can be evaluated as follows:

$$\frac{1}{N} \nabla_{\parallel} (N \vec{v}_{e\parallel}) = - \frac{1}{N e} \nabla_{\parallel} J_{\parallel}.$$

Now  $J_{\parallel}$ , the parallel current is given by the following expression:

$$J_{\parallel} = \frac{c}{4\pi} e_{\theta} \cdot [\nabla \times (e_{\theta} \times \nabla \psi)] = \frac{c}{4\pi} \nabla_{\perp}^2 \psi.$$

Adding the contributions due to all the terms together, Eq. (A7) can be written as

$$\begin{aligned} \frac{\partial n}{\partial t} - (V_n - V_g) \frac{\partial \phi}{\partial Z} - V_g \frac{\partial n}{\partial Z} + e_{\theta} \times \nabla \phi \cdot \nabla n \\ - V_A^2 \{ \nabla_{\parallel 0} \nabla_{\perp}^2 \psi + e_{\theta} \times \nabla \psi \cdot \nabla \nabla_{\perp}^2 \psi \} = 0. \end{aligned} \quad (\text{A9})$$

Similarly, the quasineutrality condition of  $\nabla \cdot \vec{J} = 0$  is used to obtain the evolution equation for  $\nabla_{\perp}^2 \phi$ . The current in the perpendicular direction is the difference between the ion and electron drifts. Using the ordering scheme as before the normalized equation can be obtained as

$$\begin{aligned} \frac{\partial}{\partial t} \nabla_{\perp}^2 \phi - V_g \frac{\partial n}{\partial Z} + e_{\theta} \times \nabla \phi \cdot \nabla \nabla_{\perp}^2 \phi - V_A^2 \{ \nabla_{\parallel 0} \nabla_{\perp}^2 \psi + e_{\theta} \\ \times \nabla \psi \cdot \nabla \nabla_{\perp}^2 \psi \} = 0. \end{aligned} \quad (\text{A10})$$

The parallel component of electron momentum equation yields upon retaining terms up to order  $\delta^2$

$$\frac{\partial \psi}{\partial t} + \nabla_{\parallel 0} (n - \psi) + e_{\theta} \times \nabla \psi \cdot \nabla (n - \phi) = \eta J_{\parallel} \quad (\text{A11})$$

after appropriate normalizations mentioned in the text of the manuscript. Here  $E_{\parallel} = \nabla_{\parallel} \phi - (1/c) \partial \psi / \partial t$  has been used.

For perturbation scale lengths much smaller than the system size along  $Z$  the infinite cylindrical shell representation

is reasonably valid for a toroidal assembly. We finally, make use of the standard transformation which takes the cylindrical shell to a slab form, which is valid in the limit of large radius of the cylindrical shell compared with the shell width. We use the following coordinate transformations,  $x=r$ ,  $y=-Z$ , and  $z=R_0\theta$ . Applying this standard transformation to Eqs. (A9), (A10), and (A11) we obtain the three model set of equations, viz., Eqs. (1), (2), and (3) considered in the text. Also note that the expression given by Eq. (A4) matches under this transformation to the expression of the equilibrium magnetic field used in the text.

<sup>1</sup>A. Das, A. Sen, S. Mahajan, and P. Kaw, Phys. Plasmas **8**, 5104 (2001).

<sup>2</sup>A. Das, S. Mahajan, P. Kaw, A. Sen, S. Benkadda, and A. Verga, Phys. Plasmas **4**, 1018 (1997).

<sup>3</sup>A. Hasegawa and M. Wakatani, Phys. Rev. Lett. **59**, 1581 (1987).

<sup>4</sup>Z. Lin, T. S. Hahm, W. W. Lee, W. M. Tang, and R. B. White, Science **281**, 1835 (1998).

<sup>5</sup>G. Hammet, M. Beer, W. Dorland, S. C. Cowley, and S. A. Smith, Plasma Phys. Controlled Fusion **35**, 973 (1993).

<sup>6</sup>A. M. Dimits, T. J. Williams, J. A. Byers, and B. I. Cohen, Phys. Rev. Lett. **77**, 71 (1996).

<sup>7</sup>R. D. Sydora, V. K. Decyk, and J. M. Dawson, Plasma Phys. Controlled Fusion **38**, A281 (1996).

<sup>8</sup>P. H. Diamond, M. N. Rosenbluth, F. L. Hinton *et al.*, *Plasma Physics and Controlled Nuclear Fusion Research* (International Atomic Energy Agency, Vienna, 1998).

<sup>9</sup>P. H. Diamond, M. N. Rosenbluth, E. Sanchez, C. Hidalgo, B. Van Milligan, T. Estrada, B. Branas, M. Hirsch, H. J. Hartfuss, and B. A. Carreras, Phys. Rev. Lett. **84**, 4842 (2000).

<sup>10</sup>F. H. Busse, Chaos **4**, 123 (1994).

<sup>11</sup>R. Z. Sagdeev, V. D. Shapiro, and V. I. Shevchenko, Sov. J. Plasma Phys. **4**, 306 (1978).

<sup>12</sup>P. W. Terry, Rev. Mod. Phys. **72**, 109 (2000).

<sup>13</sup>B. N. Rogers, W. Dorland, and M. Kotschenreuther, Phys. Rev. Lett. **85**, 5336 (2000).

<sup>14</sup>W. Dorland, F. Jenko, M. Kotschenreuther, and B. N. Rogers, Phys. Rev. Lett. **85**, 5579 (2000).

<sup>15</sup>R. Singh, P. Kaw, and J. Weiland, Nucl. Fusion **41**, 1219 (2001).

<sup>16</sup>V. E. Zakharov, Sov. Phys. JETP **35**, 908 (1972).

<sup>17</sup>S. Chandrasekhar, *Hydrodynamics and Hydromagnetic Stability* (Oxford University Press, London, 1961).

<sup>18</sup>P. K. Shukla, M. Y. Yu, H. V. Rahman, and K. H. Spatckek, Phys. Rep. **105**, 228 (1984), see discussion on p. 323.

<sup>19</sup>A. Hasegawa and M. Wakatani, Phys. Rev. Lett. **50**, 682 (1983).

<sup>20</sup>B. B. Kadomtsev and O. P. Pogutse, Rev. Plasma Phys. **5**, 249 (1970).

<sup>21</sup>D. Bora, Phys. Lett. A **139**, 308 (1989); G. Prasad, D. Bora, and Y. C. Saxena, Geophys. Res. Lett. **19**, 241 (1992).

<sup>22</sup>P. N. Guzdar, J. F. Drake, D. McCarthy, A. B. Hassam, and C. S. Liu, Phys. Fluids B **5**, 3712 (1993).

<sup>23</sup>A. Zeiler, D. Biskamp, J. F. Drake, and P. N. Guzdar, Phys. Plasmas **3**, 2951 (1996).

<sup>24</sup>B. N. Rogers and J. F. Drake, Phys. Rev. Lett. **79**, 229 (1997).

<sup>25</sup>B. N. Rogers, J. F. Drake, and A. Zeiler, Phys. Rev. Lett. **81**, 4396 (1998).